Available online at www.sciencedirect.com
ScienceDirect
International Journal of Heat and Mass Transfer 50 (2007) 4243–4255
International Journal of HEAT and MASS TRANSFER
www.elsevier.com/locate/ijhmt

An investigation into fixed-bed microreactors using lattice Boltzmann method simulations

P.-H. Kao, T.-F. Ren, R.-J. Yang *

Department of Engineering Science, National Cheng Kung University, Tainan 70101, Taiwan

Received 24 September 2006; received in revised form 16 February 2007
Available online 2 May 2007

Abstract

The fixed-bed microreactor is an important component in many biochip, microsensor, and microfluidic devices. The lattice Boltzmann method (LBM) provides a powerful technique for investigating such microfluidic systems. Accordingly, this study performs LBM-based simulations to examine fluid flows through a fixed-bed microreactor comprising a microarray of porous solids. During operation, the fluid and porous solid species are heated to prompt the chemical reaction necessary to generate the required products. Using the LB model, the flow fields and temperature fields in the microreactor are simulated for different Reynolds numbers, heat source locations, the reacting block aspect ratios, and porosity. A simple model is proposed to evaluate the chemical reactive efficiency of the microreactor based on the steady-state temperature field. The results of this model enable the optimal configuration and operating parameters to be established for the microreactor.

Keywords: Microreactor; Porous media; Lattice Boltzmann method (LBM)

1. Introduction

Microreactors play a key role in many biosensor and microfluidic applications and have been the subject of many experimental and theoretical studies. Aoki and Hasebe et al. [1] used a set of dimensionless geometric design factors to examine the microreactors. These geometric design factors were utilized to arrange the fluid segments of reactor inlet and to determine the cross-sectional shape of the fluid segments. These dimensionless factors enable to predict the reactor performance for any given set of geometric design factors. Or inversely, the dimensionless numbers provide the means to determine the geometric design factors of the fluid segments required to obtain the desired reactor performance. Masuda and Suzuki et al. [2] developed numerical solutions for the heat and fluid flows in the T-junction region of a supercritical microreactor. The authors showed that a nonlinear k–ε model with the low Reynolds number effect was the appropriate computational method for their cases. Microreactors effectively enhance the product selectivity of extremely fast exothermic reactions. Furthermore, micromixing enhances the selectivities of competitive parallel reactions and competitive consecutive reactions [3]. Previous studies of microfluidic systems and biosensor devices with a reaction function generally assumed the microreactor to be a fixed-bed type designed in the form of a microarray of porous solids. Investigating the heat and fluid flows in such systems requires a powerful tool capable of performing pore-scale analysis and not restricted by the hydrodynamic continuum condition.

The kinetic-based lattice Boltzmann method (LBM) has emerged as a promising numerical technique for simulating fluid flows and modeling the physics in fluids [4–7]. Many lattice Boltzmann (LB) models have been proposed for analyzing the problem of fluid flow through porous media. Spaid and Phelan [8] proposed a LB model for simulating fluid flow in fibrous porous media. In their approach, the Brinkman equation was recovered by modifying the particle

* Corresponding author. Tel.: +886 6 200 2724; fax: +886 6 276 6549.
E-mail address: rjyang@mail.ncku.edu.tw (R.-J. Yang).

0017-9310/$ - see front matter © 2007 Elsevier Ltd. All rights reserved.
doi:10.1016/j.ijheatmasstransfer.2007.02.031

Nomenclature

AR	aspect ratio $AR \equiv H^*/W$, where H^* and W are the height and width of porous block for microreactors
c_i	microscopic particle velocity in each lattice link i
c_s	speed of sound
Da	Darcy number
f	distribution function for the flow field
g	distribution function for the temperature field
H	height of channel
k	permeability of the porous medium
L	length of channel
$\overline{L}$	flow path length of the porous medium
L^*	unit length of computational domain for local pore structure
Nu	Nusselt number
Pr	Prandtl number
PRF	integral porous reacting fraction
Re	Reynolds number for channel
Re_D	Darcy Reynolds number inside porous medium
Re_F	flux Reynolds number for porous boundary
SR^*	local surface reacting ratio
T	temperature
$\overline{U}$	mean velocity (Darcy flux) within porous medium
T_{att}	temperature of effective activation energy for chemical reaction
t	macroscopic time
u_A	macroscopic flow velocities, where subindex A is the components of Cartesian coordinates
u_i	injection velocity normal to porous boundaries
u_W	sliding upper wall velocity for Couette flow

Greek symbols

α	thermal diffusivity
Δt	time interval (step) of LBM
ϕ	porosity of porous medium
ν	kinetic viscosity
ρ	fluid density
τ_D	relaxation time for the temperature field
τ_v	relaxation time for the flow field
ω_{OV}	overall reaction rate

equilibrium distribution function to reduce the magnitude of the momentum at specified lattice sites for porous regime while leaving the direction of the momentum unchanged. Alazmi and Vafai [9] conducted a detailed analysis of various fluid flow and heat transfer conditions at the interface between a porous medium and a fluid layer. Martys [10] presented a new approach for generalizing the LBM to ensure fluid flow consistent with those of the Brinkman equation. In this literature, a lattice Boltzmann model is proposed for isothermal incompressible flow in porous media. The key point is to include porosity into equilibrium distribution, and to add a force term to the evolution equation to account for the linear and nonlinear drag forces of the medium [11]. Zeiser and Lammers et al. [12] employed a LB automata to study the behavior of a reacting, viscous flow within the complex geometry of a fixed-bed reactor. Recent study for convection heat transfer in porous media has also been proposed [13].

The present study uses LBM-based simulations to investigate the characteristics of a 2-D porous type microreactor with a microarray structure, as shown in Fig. 1. Specifically, the simulations investigate the heat and fluid flows in the microreactor for different operational and geometric conditions, including the Reynolds number (Re) of the channel flow, the position of the heat source, and the aspect ratio (AR) and porosity (ϕ) of the reacting block. Additionally, a simple model is proposed to evaluate the chemical reactive efficiency of the microreactor based on the steady-state temperature distribution. This model avoids the requirement for time-consuming iterative calculations and provides a straightforward means of identifying the optimal operational and geometric parameters of the microreactor.

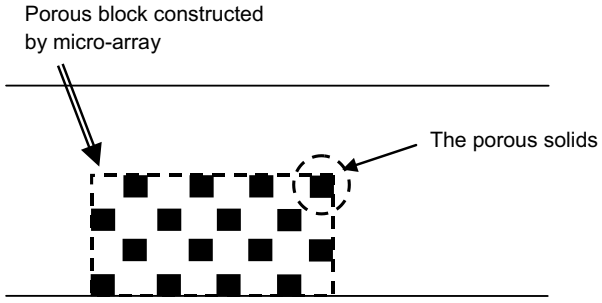

Fig. 1. Fixed-bed microreactor comprising microarray of porous blocks.

2. Numerical method

2.1. Lattice Boltzmann model

In simulating the flow and temperature fields within the microreactor using the LBM, the following assumptions are made:

(1) No external body forces (e.g. buoyancy) are applied to the flow field.
(2) The flow is incompressible in the low Reynolds number regime, and hence the effects of viscous heat dissipation can be neglected.
(3) Radiative heat transfer is ignored.
(4) The flow field is unaffected by the chemical reaction process or by the heat transfer. Hence, the flow field

and temperature field can be decoupled and solved separately.

(5) The chemical reaction does not influence the temperature field, i.e. there is very little or negligible heat generated/absorbed during the chemical reaction process. Hence, the temperature field and the chemical reaction can be decoupled and solved separately.

The LB model of the microreactor is based on two distribution functions, f and g, relating to the flow field and the temperature field, respectively. The density and temperature distribution functions are defined as the probability of particles at site x on time t moving with the particle velocity c_i during the time interval Δt in each lattice direction (link) i. Similar models have also been proposed in [14–16]. Both distribution functions obey their respective lattice Boltzmann transport equations with the single relaxation Bhatnagar–Gross–Krook (BGK) approximation, i.e.:

$$f_i(x + c_i\Delta t, t + \Delta t) - f_i(x,t) = \frac{\Delta t}{\tau_v}[f_i^{\mathrm{eq}}(x,t) - f_i(x,t)]$$

for the flow field (1)

$$g_i(x + c_i\Delta t, t + \Delta t) - g_i(x,t) = \frac{\Delta t}{\tau_D}[g_i^{\mathrm{eq}}(x,t) - g_i(x,t)]$$

for the temperature field (2)

where τ_v and τ_D are the relaxation time for the flow and temperature lattice Boltzmann equations (LBEs) respectively, and $c_s = 1/\sqrt{3}$ is the speed of sound. The kinetic viscosity, ν, and thermal diffusivity, α, are related to their corresponding relaxation time via the expressions: $\nu = c_s^2(\tau_v - 1/2)$ and $\alpha = c_s^2(\tau_D - 1/2)$.

The local equilibrium distributions are given by [17]:

$$f_i^{eq}(x,t) = w_i\rho\left[1 + \frac{c_{iA}\cdot u_A}{c_s^2} + \frac{u_A u_B}{2c_s^2}\left(\frac{c_{iA}c_{iB}}{c_s^2} - \delta_{AB}\right)\right]$$

for the flow field (3)

$$g_i^{eq}(x,t) = w_i T\left[1 + \frac{c_{iA}\cdot u_A}{c_s^2} + \frac{u_A u_B}{2c_s^2}\left(\frac{c_{iA}c_{iB}}{c_s^2} - \delta_{AB}\right)\right]$$

for the temperature field (4)

In these expressions, the flow properties are defined as:

$$\text{Flow density: } \rho = \sum_i f_i \quad (5)$$

$$\text{Momentum flux: } \rho u_A = \sum_{iA} f_i c_{iA} \quad (6)$$

$$\text{Temperature population: } T = \sum_i g_i \quad (7)$$

Note that sub-indices A and B are the components of Cartesian coordinates with implied summation for repeated indices. Additionally, w_i is the weighting which can be determined to achieve isotropy of forth-order tensor of velocities and Galilean invariance [18].

As stated in the assumptions, the flow field and the temperature field are decoupled. Therefore, the present simulations commence by solving LB Eq. (1) to obtain the steady-state flow field, and then apply LB Eq. (2) to solve the corresponding temperature distribution. Finally, a simple model is employed to estimate the chemical reactive efficiency of the microreactor based on the steady-state temperature distribution. It shall be noted that this chemical reacting model is not solved by the LBM, hence the simulations for species concentration is not required.

Using the Chapman–Enskog expansion, the continuity equation and the Navier–Stokes equations can be recovered exactly at the second-order approximation from LB Eq. (1) if the density variation is small enough [19]:

$$\frac{\partial\rho}{\partial t} + \nabla\cdot(\rho\mathbf{u}) = 0 \quad (8)$$

$$\frac{\partial(\rho\mathbf{u}_A)}{\partial t} + \nabla_A\cdot(\rho\mathbf{u}_A\mathbf{u}_B) = -\nabla_A(c_s^2\rho) + \nu\nabla_B\cdot(\nabla_A\rho\mathbf{u}_B + \nabla_B\rho\mathbf{u}_A) \quad (9)$$

Similarly, the convective-diffusive equation can be obtained from the LB equation of the temperature field, Eq. (2), as derived in [20]:

$$\frac{\partial T}{\partial t} + (\mathbf{u}\cdot\nabla)T = \nabla\cdot(\alpha\nabla T) \quad (10)$$

where T is the temperature population, expressed as a dimensionless temperature in the range $0 \leqslant T \leqslant 1$.

The present LB simulations are based on the D2Q9 model, i.e. two-dimensional nine-velocities model, and hence the relative weightings for Eqs. (3) and (4) are given by: $w_i = 4/9$ for $|c_i| = 0$ (for the static particle), $w_i = 1/9$ for $|c_i| = 1$, and $w_i = 1/36$ for $|c_i| = \sqrt{2}$. Regarding the flow field boundary condition, the bounce-back scheme is applied for all no-slip solids, which include the channel walls and the surface of the solids within the porous block. This scheme simply specifies the outgoing directions of the distribution function as the reverse of the incoming directions at each boundary site to invert the momentum at solid walls. For the channel flow simulation, the inflow boundary condition is given by a specified velocity profile, e.g. the fully-developed analytical solution of Poiseuille flow, so that the inflow distribution functions (f) can be computed according to Eq. (3). Furthermore, the flow distribution functions for channel outlet are determined by the "porous plug" boundary condition for open channel as proposed in [6], in which the unknown distribution functions at outlet are calculated and partially reversed according to mass (particle) conservation within the computational domain.

Regarding the temperature field, adiabatic walls are formulated by using an extrapolation scheme to set the temperature gradient in the direction normal to the wall equal to zero, i.e. $\partial T/\partial n = 0$. Moreover, for the boundary with a constant temperature, there are several approaches presented for LBGK model. One applies the bounce-back rule of the non-equilibrium distribution function proposed by Zou and He [21] to formulate boundary models

[15,22,23]. In [24,25], the thermal equilibrium distribution functions are applied on the wall nodes in the case of known temperature, including the adiabatic wall. Present study directly employs the thermal equilibrium distribution computed from Eq. (4) on the boundary nodes with given temperature.

2.2. Analysis of chemical reactive efficiency within porous block

Since the chemical reaction in the microreactor is not computed by LB Eqs. (1) or (2), the efficiency of the chemical reaction can nevertheless be estimated by post-processing the simulation results obtained by the steady-state temperature field. In the proposed approach, the chemical reactive efficiency within the porous block is evaluated using a dimensionless local surface reacting ratio whose formulation is based on an Arrhenius representation of a sequence of one-step simple chemical reactions, i.e. $\lambda_S P_S + \lambda_F P_F \rightarrow \lambda_R P_R$, in which P is the component of the species (e.g. O_2, H_2O...), λ is the stoichiometric coefficient of the respective species, and sub-indices S, F, and R denote the porous solid, fluid and chemical reaction product species sequentially. The overall reaction rate by the Arrhenius format is given by:

$$\omega_{OV} = \kappa_{OV} C_S C_F \exp(-T_{att}/T) \tag{11}$$

where κ_{OV}, C_S, C_F, and T_{att} are the reaction coefficient, the concentrations of the porous solid, fluid, and the temperature of effective activation energy for chemical reaction, respectively. In the simulations, the temperatures in Eq. (11), i.e. T_{att} and local temperature T at the surface nodes of reacting solid inside porous block, can both be normalized by T_{att}. Then the normalized local temperature T is specified in the range $T_L \leqslant T \leqslant T_H$, where T_L is the temperature in the inlet channel of the microreactor and T_H is the temperature of the heat source. To simply this model for convenience, the values of C_S, C_F and κ_{OV} in Eq. (11) are assumed to be constant, i.e. an assumption is made that neither the solid nor the fluid species are consumed during the chemical reaction. Therefore, the local surface reacting ratio can be defined as:

$$\begin{aligned} SR^*(x,t) &\equiv \frac{(\Delta\omega_{OV})_{Local}}{(\Delta\omega_{OV})_{Ideal}} \\ &= \frac{\exp(-1/T) - \exp(-1/T_L)}{\exp(-1/T_H) - \exp(-1/T_L)} \times 100\% \end{aligned} \tag{12}$$

The ratio given in Eq. (12) estimates the efficiency of the chemical reaction by quantifying the local reaction at every reacting surface node of the porous solid as a relative fraction of the ideal reaction. This model avoids the requirement for time-consuming iterative computations. However, it only provides a relative value of the reaction rate, i.e. the diffusion of the product species is not simulated. Nonetheless, the model provides a convenient means of exploring the effect of different operational and geometric parameters on the chemical reactive efficiency of the fixed-bed microreactor. To quantify the efficiency of the chemical reaction within the porous block, this study defines the following integral porous reacting fraction (PRF) parameter based on the surface reacting ratio given above:

$$PRF \equiv \frac{(N_P)_{SR^* \geqslant 50\%}}{(N_P)_{total}} \times 100\% \tag{13}$$

where N_P is the number of surface nodes of the porous solids within the porous block. As shown, the porous reacting fraction is effectively a volume ratio based on the number of surface nodes at which a specified surface reacting condition ($SR^* \geqslant 50\%$ in the current case) is achieved.

3. Validation

Before applying the LB model to investigate the heat and flow fields in the microreactor, three validation cases were performed. Because the LBM has been validated for the problems of heat conduction [26], the first validation case considered the convective-diffusive thermal problem by Couette flow with porous injection boundaries. In the simulations, as shown in Fig. 2a, the lower-stationary wall of the computational domain was assigned a constant temperature of $T_L = 0$ (i.e. the minimum temperature) while the upper-moving wall with a constant sliding velocity u_W was assigned a constant temperature of $T_H = 1$ (i.e. the maximum temperature). The sidewalls were assigned the periodic boundary condition. Both upper and lower porous boundaries have the normal flux with a constant injection velocity u_i. The analytical solutions of x-component velocity profile and temperature profile for this problem have these forms respectively [15]:

$$\frac{u}{u_W} = \frac{e^{(Re_F \cdot \frac{y}{H})} - 1}{e^{(Re_F)} - 1}, \tag{14}$$

and

$$\frac{T - T_L}{T_H - T_L} = \frac{e^{(PrRe_F \cdot \frac{y}{H})} - 1}{e^{(PrRe_F)} - 1} \tag{15}$$

where Re_F is the flux Reynolds number for the porous upper/lower boundaries which is defined as $Re_F \equiv u_i L/v$ where L is the channel length, Pr is the Prandtl number $Pr \equiv v/\alpha$, and H is the channel height. Fig. 2b shows that the steady state solutions in range of the $10 \leqslant Re_F \leqslant 100$ obtained using the present flow LB model, i.e. Eq. (1), for the velocity profiles are in good agreement with the analytical solution calculated from Eq. (14). The deviation between the two solutions is found to be less than 1.03%. Once the steady state solutions of flow field are obtained, the thermal LB model, i.e. Eq. (2), can be applied sequentially to get the thermal solutions. Fig. 2c shows that the steady temperature profiles at different Re_F are also in good agreement with the analytical solution calculated from Eq. (15). The maximum deviation between the two solutions is

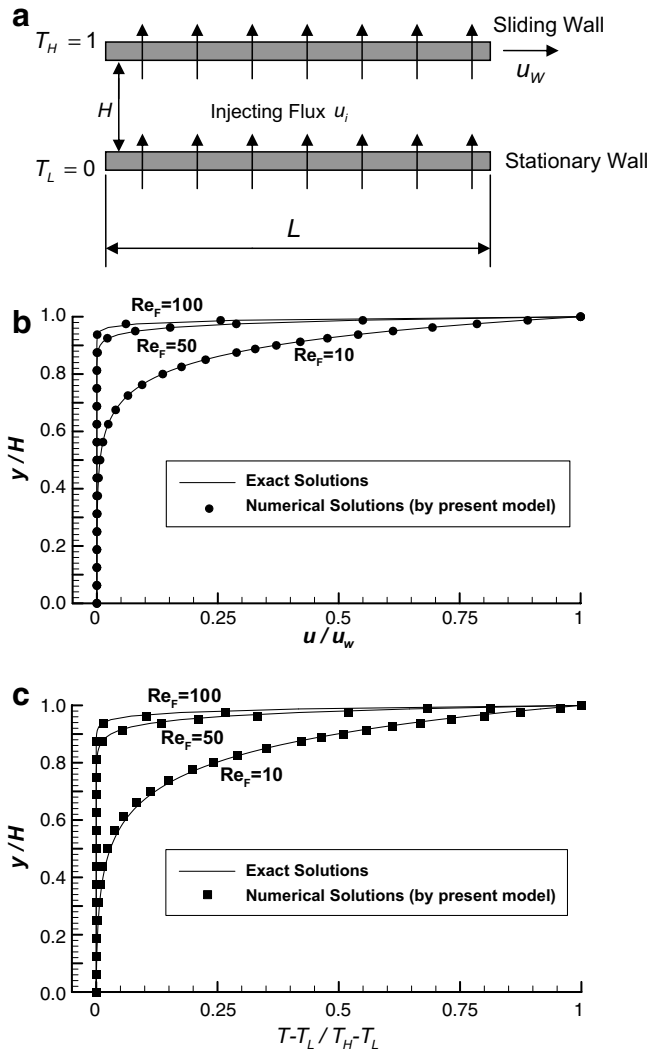

Fig. 2. Validation case for the convective-diffusive thermal problem: (a) schematic of Couette flow with porous injection boundaries, (b) analytical and LBM solutions for x-component velocity profile along y-direction, and (c) analytical and LBM solutions for temperature profile along y-direction.

2.12%. Hence, present results of this validation case have demonstrated that the current simplified LB model, which calculates the flow filed and the temperature field independently, can be utilized for the convective-diffusive thermal problems with flows at moderate Reynolds numbers.

Since the microreactor simulations consider the case of creeping flow through a porous medium, two further validation trials with grid-independence study were performed in which the results of the proposed LB model were compared to the analytical solutions obtained from the 1-D Darcy law, and to the solutions obtained for creeping flows inside the local porous structure, respectively.

For 1-D creeping flow through a porous medium, the mean velocity $\overline{U}$ (also known as the Darcy flux) is given by the 1-D Darcy law as:

$$\overline{U} = \frac{k \cdot \Delta p}{\nu \cdot \rho \cdot \overline{L}} \tag{16}$$

where Δp is the pressure difference between the inlet and the outlet of the porous medium, ν is the kinetic viscosity, ρ is the density of the fluid, $\overline{L}$ is the flow path length of the porous medium, and k is the permeability.

In the problem of 1-D creeping flow through a porous medium, the Darcy Reynolds number is defined as $Re_D = \overline{U}d/\nu\phi$, where d is the average diameter of the porous solids (particles) which can be evaluated by the relationship of square porous solid with side-length (l_S) such that $d = (4 \cdot l_S^2/\pi)^{0.5}$, and ϕ is the porosity of the porous medium through which the fluid flows. For creeping flow, Ergun [27] showed that the permeability k and porosity ϕ are related by $k = \frac{d^2\phi^3}{150(1-\phi)^2}$. Theoretically, the 1-D Darcy law given in Eq. (16) is valid only for creeping flow, i.e. for which the Darcy Reynolds number Re_D is less than 10. To validate the performance of the proposed LB model in solving the 1-D Darcy problem, the computational domain shown in Fig. 3a was constructed with parameters of $d = 3.3857$, $L = 100$, and $\phi = 74.72\%$. In accordance with Ergun's model, the permeability was calculated to be $k = 0.50$. The flow properties ν and ρ were assigned values of given relaxation time τ_v for the flow field and the initial density distribution function f, respectively. The mean velocity in the porous medium, $\overline{U}$, and the pressure difference between the inlet and the outlet of the porous medium, Δp, were then calculated at various Darcy Reynolds numbers within the creeping flow regime ($Re_D \leqslant 10$) using the LB model. The results for the mean velocity were then compared with those obtained from the 1-D Darcy law given in Eq. (16). The corresponding results are summarized in Table 1. From inspection, it is found that the deviation between the two sets of results is less than 2%. The current results in this validation case have shown that the present LB model can simulate the fluid flows through a porous medium in macroscopic (global) scale with creeping flow condition ($Re_D \leqslant 10$) even the coarse grid size is used.

However, for porous medium flow simulations, Pan and Luo et al. [28] proposed that the LB model with single-relaxation BGK collision and standard bounce-back scheme applied to no-slip solid nodes arises some numerical problems, such as the viscosity-dependent effect for no-slip boundary and numerical errors in estimation of local permeability for porous media. Based on this reason, the third validation trial considered the case of fluid flow through a local (microscopic) pore structure, as shown in Fig. 3b. The geometrical ratio of the computational domain for local pore structure is fixed as $2L^*/L^* = 2.0$, and a lower porosity ($\phi = 65\%$) is taken into account. The simulations in present validation case are performed using various grid numbers from $N = 20$–100 per unit L^* within the creeping flow regime $Re_D \leqslant 10$.

Fig. 4a presents the results of estimated value of dimensionless local permeability k/k^* against the different relaxation time (τ_v) at $Re_D = 1.0$, where the k^* is the reference local permeability which is obtained numerically at $Re_D = 10^{-2}$. The results exhibited in Fig. 4a show that: when over-relaxation is utilized, i.e. $\Delta t/\tau_v > 1$ for Eq. (1)

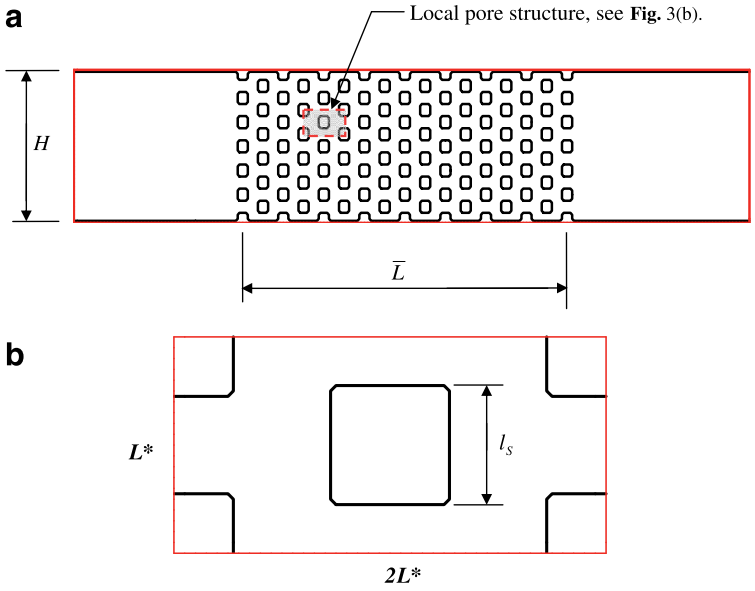

Fig. 3. (a) Schematic of porous channel in problem of fluid flow described by 1-D Darcy law, and (b) schematic of local pore structure in problem of fluid flow in microscopic scale with grid-independence study.

Table 1
Comparison of LBM results and 1-D Darcy law solutions for mean flow velocity in porous medium

Re_D	$\overline{U}$ by LBM	$\overline{U}$ by 1-D Darcy's law	Deviation (%)
0.1	1.9369×10^{-4}	1.9358×10^{-4}	5.816×10^{-2}
0.5	9.7234×10^{-4}	9.6823×10^{-4}	0.425
0.8	1.5599×10^{-3}	1.549×10^{-3}	0.672
1	1.9518×10^{-3}	1.9358×10^{-3}	0.823
1.5	2.9441×10^{-3}	2.9105×10^{-3}	1.155
2	3.9364×10^{-3}	3.8814×10^{-3}	1.417
3	5.9085×10^{-3}	5.8073×10^{-3}	1.742
6	1.2031×10^{-2}	1.1868×10^{-2}	1.375
9	1.7811×10^{-2}	1.7489×10^{-2}	1.844

by the case of $\tau_v = 0.6$, the accuracy can be obviously improved by using the finer grid size. Fig. 4b displays the estimated local k/k^* values using various grid size at different Re_D when $\tau_v = 0.6$. It can be observed that, when over-relaxation is employed, i.e. $\tau_v < 1.0$, the numerical errors of local k/k^* value can be controlled under the condition of $|\frac{k}{k*} - 1| \leqslant 5\%$ using the grid numbers $N \geqslant 20$, while the flow within a porous medium satisfies $Re_D \leqslant 1.0$. Consequently, consider the computational accuracy and efficiency, the appropriate grid system of 20×40 for the local pore structure is good enough while the fluid flow through a porous medium satisfies the condition of $Re_D \leqslant 1.0$ with over-relaxation parameter $\Delta t/\tau_v > 1$. Hence, the following simulations in present study employ this grid system to investigate the fluid flow inside a fixed-bed microreactor.

4. Results and discussion

The present simulations consider two microreactors in which the heat source is located in different positions, as shown in Fig. 5. In Case 1, the heat source is located directly beneath the porous block, while in Case 2, the heat source is located immediately in front of the porous block. In both cases, the width and height of the porous block are denoted by W and H^*, respectively, and the height of the channel is given by H. In the simulations, the width of the porous block is fixed at one half of the channel height, i.e. $W = H/2$, but the height of porous block is varied to give different values of the aspect ratio, $AR \equiv H^*/W$.

According to results by our previous validation cases, the over relaxation factor for flow field is utilized such as $1/\tau_v = 1.9$ as a constant, so that a fixed value of $\tau_v = 0.5263$ can be determined. The channel Reynolds number, which is $Re \equiv \frac{\bar{u}_{in} H}{\nu}$ where $\bar{u}_{in}$ is the mean velocity at channel inlet, can also be specified according the specific value of $\bar{u}_{in}$. For present study, the inflow velocity is given as the analytical parabolic profile of Poiseuille flow based on specific $\bar{u}_{in}$, such as $u_{in} = 1.5 \cdot \bar{u}_{in}[1 - (y - 0.5H)^2/0.25H^2]$. Meanwhile, once the Prandtl number is set as 0.71, the relaxation time for temperature field can be obtained as $\tau_D = 0.5371$.

The efficiency of the chemical reaction in the microreactor strongly depends on the characteristics of the thermal transfer within the porous block. In turn, these characteristics are dependent on the flow behavior in the block. This study simulates the flow and temperature fields in the Case 1 and Case 2 microreactor configurations for different values of the Reynolds number of the channel flow, i.e. $Re = 10$, 50 and 100, different porosities of the reacting block, i.e. $\phi = 85\%$ and 65%, and different aspect ratios of the reacting block, i.e. AR = 0.5, 1.0 and 1.5. The reactive efficiency of the two microreactors is then estimated and compared using the simple model formulated in Section 2.2.

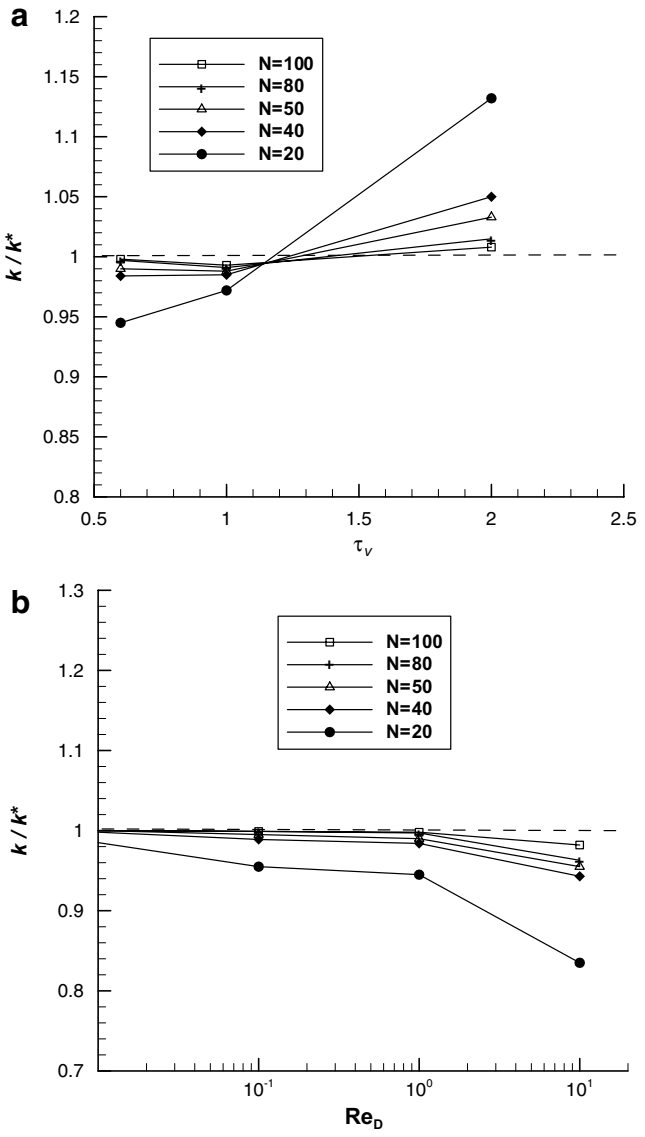

Fig. 4. LBM solutions of dimensionless permeability for creeping flow through a local pore structure, (a) dimensionless permeability against the relaxation time (τ_v) using different grid size N, and (b) dimensionless permeability at different Darcy's Reynolds number using various grid size when $\tau_v = 0.6$.

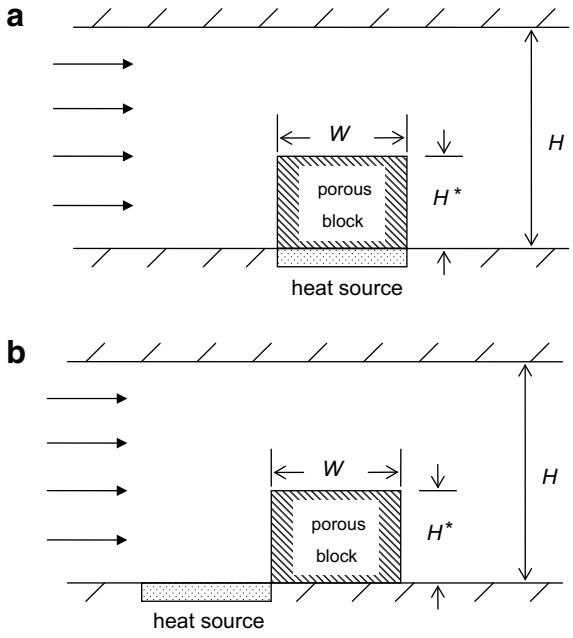

Fig. 5. Schematic of microreactors with heat source in different locations: (a) Case 1: heat source located directly beneath porous block, (b) Case 2: heat source located immediately in front of porous block.

4.1. Flow field and temperature distributions

In a fixed-bed microreactor, the temperature distribution within the porous block is strongly influenced by the flow pattern within the block. Fig. 6 presents the x-component flow velocity (u_x) profiles at different cross-sections of the porous block without considering the positions of the heat source, e.g. Case 1 and Case 2. In general, the results reveal that the flow velocities in the block increase with increasing Reynolds number and aspect ratio. It can be seen that most of the fluid in the channel flows through the non-porous regime above the reacting block. To ensure the present LB model and the employed grid system are accurate for current simulation cases, the maximum Darcy's Reynolds number is checked for each simulated case. The maximum Re_D value is found to be 0.805 occurred in the case with parameters: $\phi = 85\%$, AR = 1.5 at channel Reynolds number $Re = 100$, as the shown in Fig. 6d. Therefore, the creeping flow limitation for porous medium simulations and the numerical accuracy of present LB model with the specific grid size can be confirmed.

As shown in Fig. 6, for the case of a high block porosity ($\phi = 85\%$), the difference in flow velocity between the porous and the non-porous regimes is significantly dependent on the Reynolds number and the aspect ratio. However, the variation in the velocity within the porous block is not as great as that within the non-porous regime. These results imply that for the higher block porosity, the effects of flow convection increase significantly with increasing Reynolds number and aspect ratio. However, a porous block with a lower porosity ($\phi = 65\%$) has a greater cushioning effect for the fluid flows, and hence the flow velocities within the porous block are less dependent on the Reynolds number and aspect ratio than in the higher porosity case. Therefore, it can be inferred that flow convection plays a less dominant role in determining the thermal transfer within the block as the porosity of the block is reduced.

When the heat source is located beneath the porous block, i.e. Case 1, it is desirable that the thermal energy produced by the heat source should be transferred as far as possible towards the upper surface of the porous block via thermal diffusion, while the drift of thermal energy downstream away from the block via thermal convection should be minimized. Under these conditions, a higher and more uniform temperature distribution is obtained

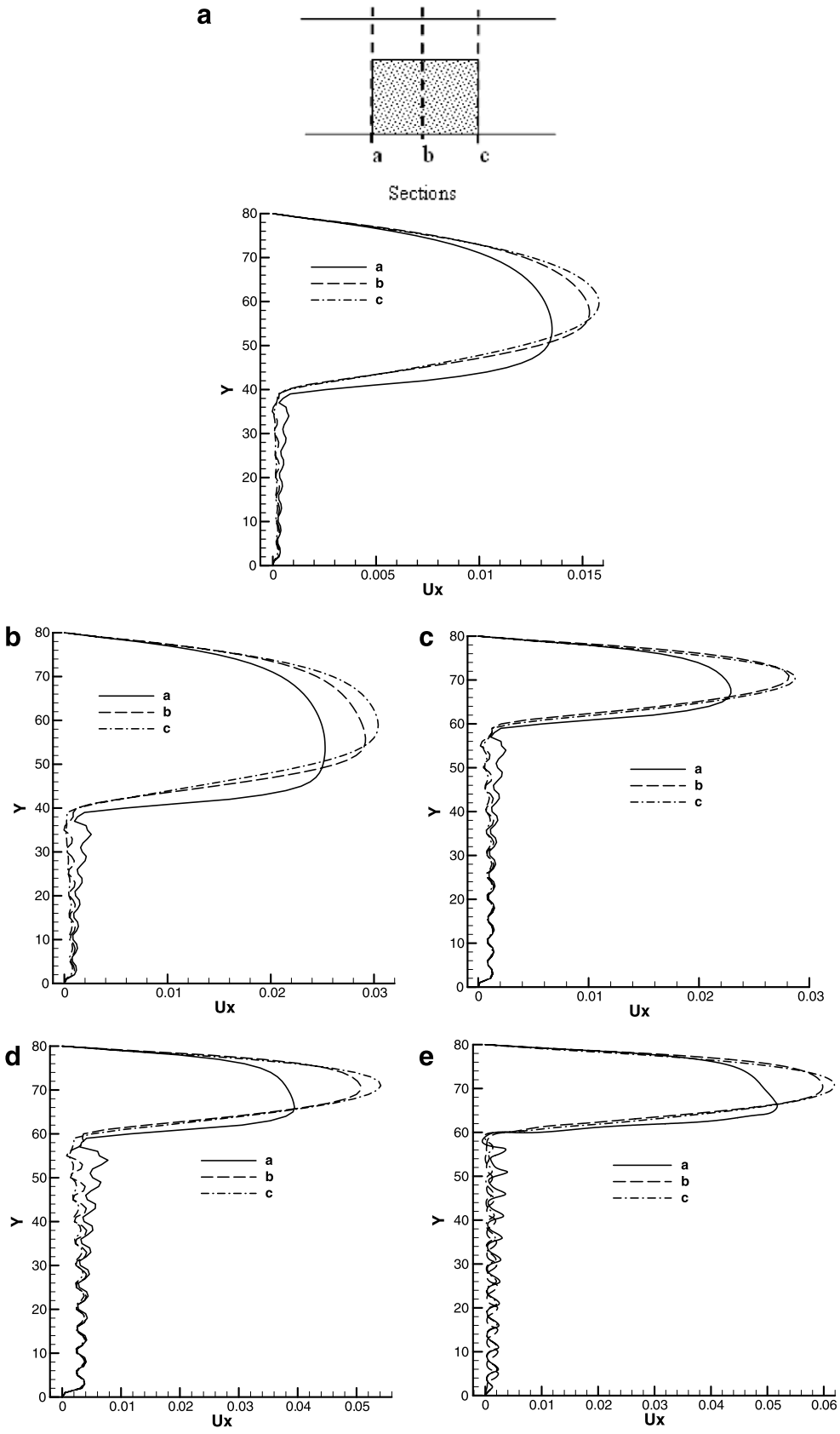

Fig. 6. Simulation results for x-velocity profiles along y-direction at different sections of porous block at various operating parameters: (a) $\phi = 85\%$, AR = 1.0, $Re = 50$; (b) $\phi = 85\%$, AR = 1.0, $Re = 100$; (c) $\phi = 85\%$, AR = 1.5, $Re = 50$; (d) $\phi = 85\%$, AR = 1.5, $Re = 100$; and (e) $\phi = 65\%$, AR = 1.5, $Re = 100$.

within the porous block, and hence the reactive efficiency is improved. However, when the heat source is located in front of the porous block, i.e. Case 2, it is desirable that the thermal energy should be transported as far along the y-direction as possible initially and then blown into the block via flow convection. Hence, it is apparent that the locations of the heat source in Case 1 and Case 2 require the different flow behaviors and thermal transfer mechanisms to obtain a uniform and higher average temperature distribution within the porous block for favorable reactive results.

Fig. 7 presents the simulated temperature contours for Case 1 for various operational and geometric conditions. Fig. 7a and b shows that at a low Reynolds number (less convection effect of flow), a higher block porosity ($\phi = 85\%$) results in a more uniform temperature distribution and a higher average temperature within the porous block. This result implies that the block with higher porosity increases the flow convection effect and reduces the thermal diffusion inside porous block. Moreover, the porous solids in the microarray obstruct the diffusion of the thermal energy from the heat source towards the upper surface of the block at lower Reynolds number, and hence at a lower porosity ($\phi = 65\%$), the temperature gradient is relatively large beneath the porous block and near the heat source. Fig. 7c and d shows that the average temperature within the block reduces and becomes non-uniform at a higher Reynolds number as a result of an increased flow convection effect. In general, the results of Fig. 7 show that in Case 1, the thermal transfer within the porous block is determined primarily by the effect of flow convection, represented by the Reynolds number. And it should be note that, the aspect ratio of the porous block also influences the extent of thermal diffusion since the diffusive path is longer at higher aspect ratios.

Fig. 8 shows the simulated temperature contours and flow vectors for Case 2 at a Reynolds number of $Re = 100$ and an aspect ratio of AR = 1.5. In contrast to the previous case, it is observed that the block with a lower porosity has a higher and more uniform temperature distribution. This result suggests that the cushioning effect on flow convection is enhanced as the porosity of the reacting block is reduced in this particular configuration. Furthermore, the aspect ratio does not have a strong influence on the flow behavior within the porous block and hence the AR parameter has no significant effect on the thermal transfer. Fig. 8a2 and b2 presents the velocity vectors in and around the porous block at high and low block porosities, respectively. It can be seen that a circulating flow is formed explicitly in the region behind the porous block in the low porosity case, since the cushioning effect is enhanced. As shown in Fig. 8b1, this recirculation explicitly influences the temperature distribution (contours profiles).

To investigate the effect of the flow behavior on the thermal transport, this study utilizes the Nusselt number to express the ratio of the heat transfer within the block

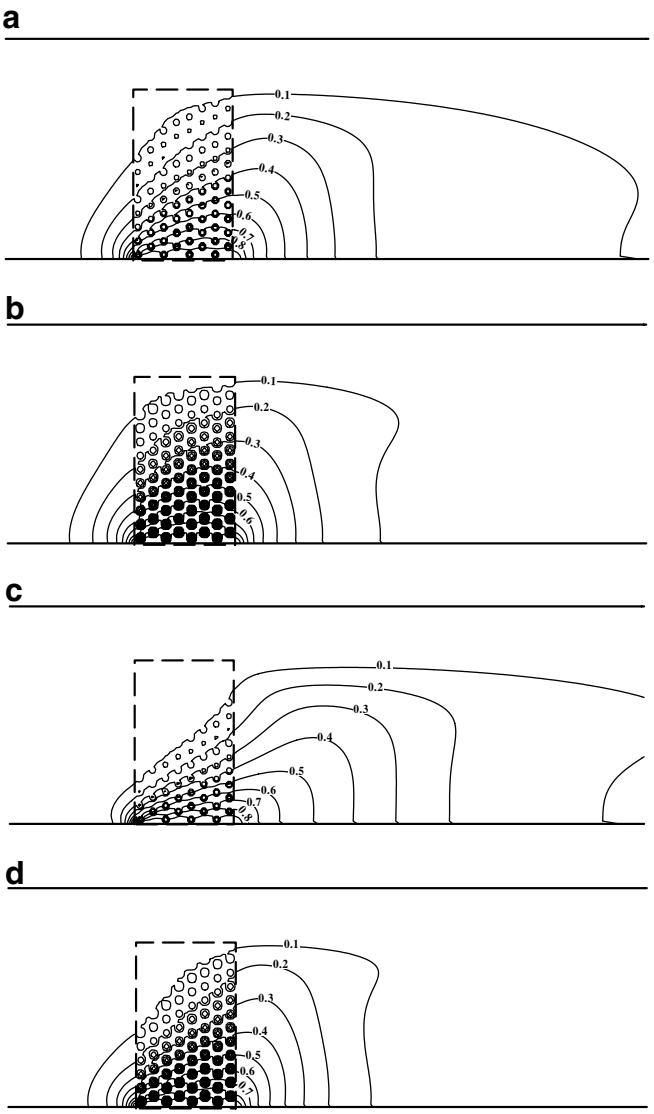

Fig. 7. Simulation results for temperature contours of Case 1 with AR = 1.5 for: (a) $Re = 50$, $\phi = 85\%$; (b) $Re = 50$, $\phi = 65\%$; (c) $Re = 100$, $\phi = 85\%$; and (d) $Re = 100$, $\phi = 65\%$.

caused by the flow behavior to that by pure thermal diffusion, i.e.

$$Nu = \frac{\dot{Q}_a}{\dot{Q}_c} = \int_{y:H^*=0}^{y:H^*=1} \int_{x:w=0}^{x:w=1} \left[(u_x T' + u_y T') - \alpha \left(\frac{\partial T'}{\partial x} + \frac{\partial T'}{\partial y} \right) \right] \mathrm{d}x\mathrm{d}y \tag{17}$$

where $\dot{Q}_a$ is the actual heat flux across the porous block, $\dot{Q}_c$ is the heat flux which would result from pure thermal conduction (i.e. diffusion), u_x and u_y denote the x- and y-components of the velocity, respectively, and T' is the local temperature at each node within the porous block. It should be noted that the Nusselt number calculation is performed only within the porous block.

Fig. 9 illustrates the variation of the Nusselt number with the Reynolds number as a function of the block porosity and aspect ratio for Case 1 and Case 2. In general,

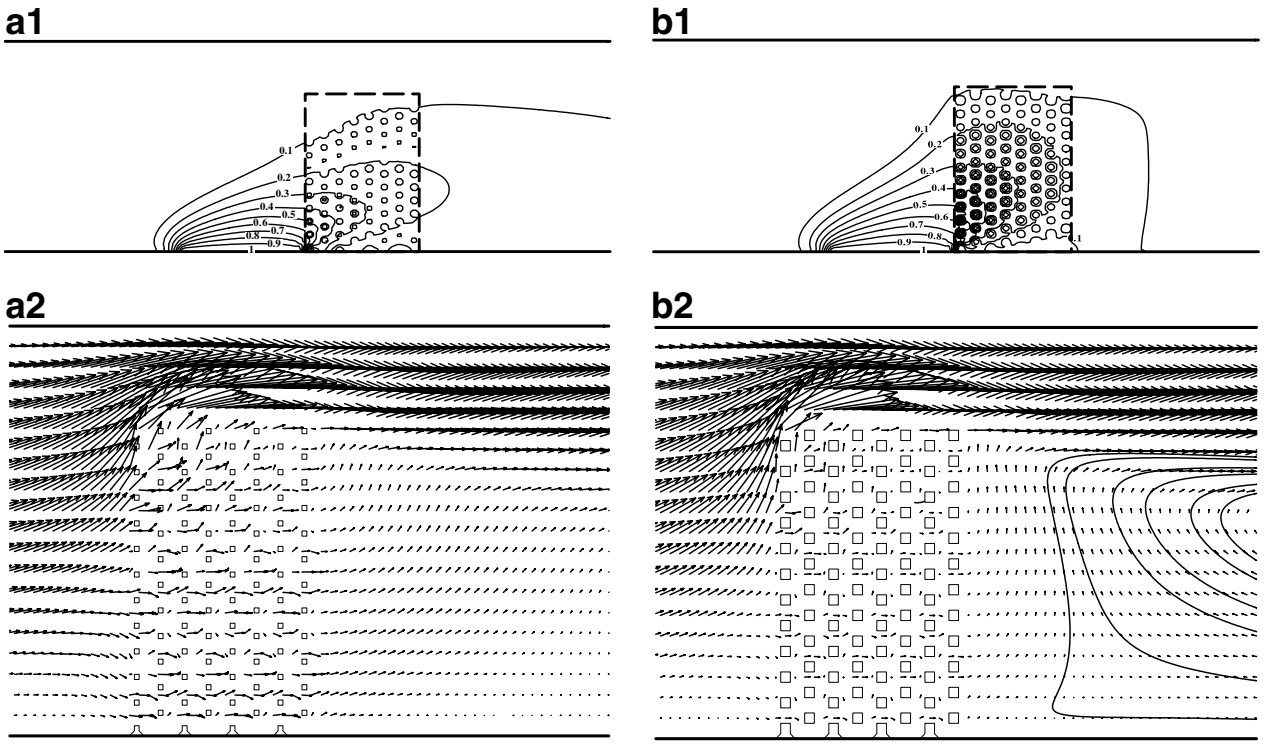

Fig. 8. Simulation results for Case 2 with AR = 1.5 and $Re = 100$: (a1) temperature contours for $\phi = 85\%$, (a2) velocity vectors for $\phi = 85\%$, (b1) temperature contours for $\phi = 65\%$ and (b2) velocity vectors with stream lines showing circulating flow behind porous block for $\phi = 65\%$.

the results show that the Nusselt number increases with increasing Reynolds number. Furthermore, the Nusselt numbers obtained at higher porosity ($\phi = 85\%$) are larger than those obtained at lower porosity ($\phi = 65\%$). Therefore, it can be inferred that the influence of flow convection on thermal transfer increases at higher Reynolds numbers and block porosities. Fig. 9b shows that in Case 2, the slop of the Nusselt-Reynolds curves become increasingly steep at higher Reynolds numbers and block porosities. This result implies that flow convection has a particularly significant effect on the thermal transfer in this particular configuration in Case 2.

4.2. Estimated efficiency of chemical reaction

In microreactor applications, the efficiency of the chemical reaction is strongly dependent on the temperature distribution within the porous block. In the present study, the simple integral porous reacting fraction (PRF) model formulated in Section 2.1. is used to estimate the chemical reactive efficiency based on the steady-state temperature distribution within the porous block.

Table 2 summarizes the PRF values calculated for reactive blocks of various aspect ratios as a function of the Reynolds number and the block porosity. Meanwhile, Fig. 10 plots the variation of the PRF value with the Reynolds number as a function of the aspect ratio and the porosity value.

In Case 1, an improved chemical reactive efficiency is obtained by increasing the diffusive effect within the reacting block while limiting the flow convection effect. Fig. 10a and Table 2a–c shows that in Case 1, the chemical reactive efficiency is enhanced at a lower Reynolds number and a lower aspect ratio since these conditions minimize the flow convection effect. Furthermore, the results show that a lower reactive efficiency is obtained at a lower porosity ($\phi = 65\%$), since the porous solids in the microarray obstruct the thermal diffusive path in the y-direction and hence reduce the uniformity and absolute value of the temperature field within the porous block. Moreover, Fig. 10a shows that the PRF values of the reacting block with a lower porosity do not decay as steeply at a higher Reynolds number as those of the block with a higher porosity. This result implies that the cushioning effect of the block with a lower porosity increases with increasing Reynolds number as exhibited in Fig. 7.

Fig. 10b presents the variation of the chemical reactive efficiency with the Reynolds number for Case 2 and the results differ from the chemical reactive efficiency in Case 1. In this microreactor configuration, the effect of flow convection on the thermal transfer is required to blow the thermal into the porous block. The results of Fig. 10b suggest that it is necessary to balance the effects of flow convection and thermal diffusion to enhance the reactive efficiency. At Reynolds numbers in the range $Re = 50$–100, the flow convection effect dominates the thermal transfer, and hence the efficiency of the chemical reaction is increased or maintained with the Reynolds number increasing. To explain clearly, it is observed that for a low block porosity ($\phi = 65\%$) and higher aspect ratios (i.e. AR = 1.0 and 1.5), the

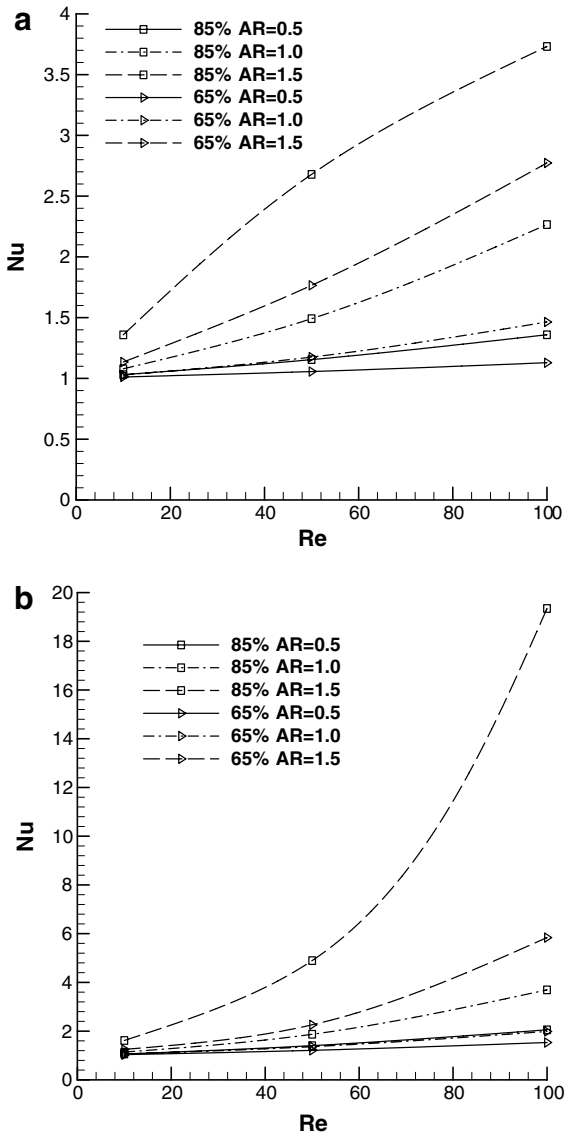

Fig. 9. Variation of Nusselt number with Reynolds number as function of porosity and aspect ratio for: (a) Case 1 and (b) Case 2.

PRF value increases as the Reynolds number increases from $Re = 50$–100 due to the increased cushioning effect. Fig. 8 has exhibited the results of the cushioning effect at different porosities as described before. For a high block porosity ($\phi = 85\%$) and a lower aspect ratio ($AR = 0.5$), the flow convection effect improves the efficiency of the chemical reaction because the upper surface of the porous block is relatively closer to the heat source in the y-direction and hence more thermal energy is transported into the block by flow convection. Therefore, it is observed that the PRF value increases slightly as the Reynolds number increases from $Re = 50$ to 100.

Finally, comparing Fig. 10a and b, it is observed that the chemical reactive efficiency of the Case 1 configuration is considerably higher than that of Case 2 for Reynolds numbers in the range $Re \leqslant 100$. Additionally, a lower aspect ratio results in a higher chemical reactive efficiency. In Case

Table 2
Values of integral porous reacting fraction (PRF) in Case 1 and Case 2 microreactors as function of porosity and Reynolds number for: (Panel a) AR = 0.5, (Panel b) AR = 1.0, and (Panel c) AR = 1.5

	ϕ	$Re = 10$	$Re = 50$	$Re = 100$
Panel a				
Case 1	85%	100%	86.72%	78.13%
	65%	96.88%	76.17%	71.88%
Case 2	85%	17.97%	10.94%	11.72%
	65%	18.36%	12.89%	11.33%
Panel b				
Case 1	85%	81.25%	59.77%	54.30%
	65%	70.51%	54.88%	51.95%
Case 2	85%	14.84%	7.81%	7.81%
	65%	17.38%	8.59%	7.81%
Panel c				
Case 1	85%	59.64%	37.24%	22.40%
	65%	54.17%	39.97%	32.29%
Case 2	85%	11.20%	7.55%	6.51%
	65%	13.93%	7.55%	9.24%

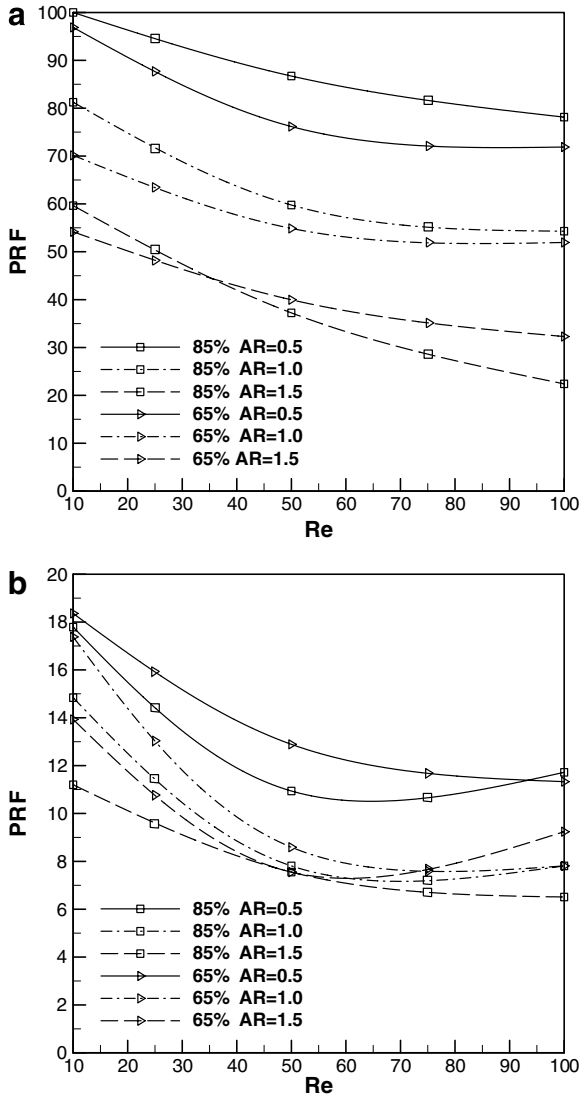

Fig. 10. Variation of integral porous reacting fraction (PRF) with Reynolds number as function of porosity and aspect ratio for: (a) Case 1 and (b) Case 2.

1, the aspect ratio of the porous block has the most significant effect on the reactive efficiency of the microreactor. For a given aspect ratio, the value of the chemical reactive efficiency is determined primarily by the porosity of the reacting block rather than by the Reynolds number of the channel flow. In Case 2, the aspect ratio, porosity of the reacting block, and the Reynolds number of the channel flow are all of approximately equal importance in terms of the effect they exert on the efficiency of the chemical reaction.

5. Conclusion

In order to investigate the heat and fluid flows in a microfluidic system, a useful and simple tool, which is capable of performing pore-scale analysis and not restricted by the hydrodynamic continuum condition, is required. For the problem of creeping flows inside a porous medium, e.g. the maximum $Re_D < 1.0$ in current cases, a simplified LBGK model with single relaxation collision and standard bounce-back scheme for no-slip boundary condition can be utilized. Three validation cases with grid-independence in Section 3 study for convective-diffusive thermal problem, global porous creeping flow in macroscopic scale, and local porous creeping flow in microscopic scale respectively, have demonstrated the suitability of present flow/thermal LB models for problems investigated in current work.

This study has performed lattice Boltzmann simulations of the steady-state flow field and temperature field in a fixed-bed microreactor for different Reynolds numbers, heat source locations, and porous block aspect ratios and porosities. The lattice Boltzmann method provides a real pore-scale simulation capability and is not restricted to the continuum flow condition. In the simulations, the fluid and porous solid species are heated to promote the chemical reaction required to generate the required product species. Detailed results for the heat transfer and fluid flow through the porous block of the reactor with different operating parameters have been presented in Section 4.1. The chemical reactive efficiency of the microreactor has then been evaluated by applying a simple mathematical model to the simulation results obtained for the steady-state temperature field.

The simulation results obtained for the Case 1 microreactor, in which the heat source is located directly beneath the porous block, have shown that an increased thermal diffusion effect and a reduced convection flow effect are preferable since these conditions maintain the majority of the generated thermal energy by the heat source keeping inside the porous block and hence improve the chemical reactive efficiency. In this configuration, the chemical reactive efficiency is enhanced at a lower Reynolds number and higher block porosity. However, the increased diffusive path should be considered at higher block porosity. In the Case 2 configuration, in which the heat source is located immediately in front of the porous block, a convective flow effect is required to drift the heat into the porous block. Thermal diffusion along the y-direction is required in front of the porous block before the heat is convected into the block, so that the flow behavior with balanced effects of thermal diffusion and flow convection is preferable in this configuration. For Reynolds numbers in the range $Re = 50$–100, the chemical reactive efficiency is enhanced at a lower aspect ratio and a higher porosity.

Base on the simulation results, the chemical reactive efficiency of the Case 1 configuration is considerably higher than that of Case 2 for Reynolds numbers in the range $Re \leqslant 100$, by this reason, the Case 1 configuration is recommended for higher efficiency applications of microreactor. For a given location of the heat source, the chemical reactive efficiency of the microreactor is governed principally by the aspect ratio of the porous block. The Reynolds number and porous block porosity exert a lesser, and broadly similar, influence. However, the simulation results have clearly shown that the chemical reactive efficiency of the microreactor is determined primarily by the location of the heat source. Specifically, it has been shown that the optimal reactive efficiency can be obtained by locating the heat source directly beneath the porous block, i.e. Case 1, and specifying a low Reynolds number channel flow and a higher block porosity.

References

[1] N. Aoki, S. Hasebe, K. Mae, Geometric design of fluid segments in microreactors using dimensionless number, AIChE 52 (2006) 1502–1515.
[2] Y. Masuda, A. Suzuki, Y. Ikushima, Calaulation method of heat and fluid flow in a microreactor for supercritical water and its solution, Int. Commun. Heat Mass Transfer 33 (2006) 419–425.
[3] J.I. Yoshida, A. Nagaki, T. Iwasaki, S. Suga, Enhancement of chemical selectivity by microreactors, Chem. Eng. Technol. 28 (2005) 259–266.
[4] S. Chen, G.D. Doolen, Lattice Boltzmann method for fluid flows, Annu. Rev. Fluid Mech. 30 (1998) 329–364.
[5] D. Yu, R. Mei, L.S. Luo, W. Shyy, Viscous flow computations with the method of lattice Boltzmann equation, Progress in Aerospace Sciences 39 (2003) 329–367.
[6] S. Succi, The lattice Boltzmann equation for fluid dynamics and beyond, Clarendon Press, Oxford, 2001.
[7] Y.G. Lai, C.L. Lin, J. Huang, Accuracy and efficiency study of lattice Boltzmann method for steady-state flow simulations, Num. Heat Transfer Part B 39 (1) (2001) 21–43.
[8] M.A.A. Spaid, F.R. Phelan, Lattice Boltzmann method for modeling microscale flow in fibrous porous media, Phy. Fluids 9 (9) (1997) 2468–2473.
[9] B. Alazmi, K. Vafai, Analysis of fluid flow and heat transfer interfacial conditions between a porous medium and a fluid layer, Int. J. Heat Mass Transfer 40 (2001) 1735–1749.
[10] N.S. Martys, Improved approximation of the Brinkman equation using a lattice Boltzmann method, Phys. Fluids 13 (6) (2001) 1807–1809.
[11] Z.Z. Guo, T.S. Zhao, Lattice Boltzmann model for incompressible flows through porous media, Phys. Rev. E 66 (2002) 036304_1–036304_9.
[12] T. Zeiser, P. Lammers, E. Klemm, Y.W. Li, J. Bernsdorf, G. Brenner, CFD- calculation of flow, dispersion and reaction in a catalyst filled tube by the lattice Boltzmann method, Chem. Eng. Sci. 56 (2001) 1697–1704.

[13] Z. Guo, T.S. Zhao, A lattice Boltzmann model for convection heat transfer in porous media, Num. Heat Transfer Part B 47 (2) (2005) 157–177.
[14] H. Yu, L.S. Luo, S.S. Girimaji, Scalar mixing and chemical reaction simulations using lattice Boltzmann method, Int. J. Comp. Eng. Sci. 3 (1) (2002) 73–87.
[15] Y. Peng, C. Shu, Y.T. Chew, Simplified thermal lattice Boltzmann model for incompressible thermal flows, Phys. Rev. E 68 (026701) (2003) 1–8.
[16] G. Barrios, R. Rechtman, J. Rojas, R. Tovar, The lattice Boltzmann equation for natural convection in a two-dimensional cavity with a partially heated wall, J. Fluid Mech. 522 (2005) 91–100.
[17] W.S. Fu, H.C. Huang, W.Y. Liou, Thermal enhancement in laminar channel flow with a porous block, Int. J. Heat Mass Transfer 39 (10) (1996) 2165–2175.
[18] Y.H. Qian, D. d'Humieres, P. Lallemand, Lattice BGK models for Navier–Stokes equation, Europhys. Lett. 17 (6) (1992) 479–484.
[19] Y.H. Qian, S.A. Orszag, Lattice BGK models for the Navier–Stokes equation: nonlinear deviation in compressible regimes, Europhys. Lett. 21 (1993) 255–259.
[20] S.P. Dawson, S. Chen, G.D. Doolen, Lattice Boltzmann computations for reaction-diffusion equations, J. Chem. Phys. 98 (1993) 1514–1523.
[21] Q. Zou, X. He, On pressure and velocity boundary conditions for the lattice Boltzmann BGK model, Phys. Fluids 9 (1998) 1591–1598.
[22] X. He, S. Chen, G.D. Doolen, A novel thermal model for the lattice Boltzmann method in incompressible limit, J. Comp. Phys. 146 (1998) 282–300.
[23] A. D'Orazio, S. Succi, Simulating two-dimensional thermal channel flows by means of a lattice Boltzmann method with new boundary conditions, Future Generation Computer Systems 20 (2004) 935–944.
[24] G.H. Tang, W.Q. Tao, Y.L. He, Simulation of fluid flow and heat transfer in a plane channel using the lattice Boltzmann method, Int. J. Mod. Phys. B 17 (1–2) (2003) 183–187.
[25] G. Barrios, R. Rechtman, J. Rojas, R. Tovar, The lattice Boltzmann equation for natural convection in a two-dimensional cavity with a partially heat wall, J. Fluid Mech. 522 (2005) 91–100.
[26] J.R. Ho, C.P. Kuo, W.S. Jiaung, C.J. Twu, Lattice Boltzmann scheme for hyperbolic conduction equation, Num. Heat Transfer Part B 41 (6) (2002) 591–607.
[27] S. Ergun, Fluid flow through packed columns, Chem. Eng. Progress 48 (1952) 89–94.
[28] C. Pan, L.S. Luo, C.T. Miller, An evaluation of lattice Boltzmann schemes for porous medium flow simulation, Comp. Fluids 35 (2006) 898–909.